CrossMark

ORIGINAL PAPER

Nitrogen-self-doped mesoporous carbons synthesized by the direct carbonization of ferric ammonium citrate for high-performance supercapacitors

Heming Luo[1] · YanZheng Chen[1] · Bing wang[1] · Jianqiang Zhang[1] · Xia Zhao[1] · Bo Mu[1]

Abstract We report a simple method of synthesizing nitrogen-self-doped mesoporous carbons by the direct carbonization of ferric ammonium citrate (FAC) in an inert atmosphere. The resulting materials stacked by nanospherical particles exhibited a large the Brunauer–Emmett–Teller (BET) surface area of up to 1021 m^2 g^{-1}, bimodal porosity (pores centered at approximately 2 and 9 nm), and nitrogen self doping (3.86 %). The electrochemical properties of the nitrogen-self-doped mesoporous carbons were evaluated in 1 M H_2SO_4 aqueous solutions by cyclic voltammetry (CV), galvanostatic charge/discharge (GCD), and electrochemical impedance spectroscopy (EIS). Results showed that FBNC-700 (FB represents FAC brown (CAS Reg. No. 1332-98-5), N represents "nitrogen-self-doped," C represents mesoporous-carbon materials, and 700 represents carbonization temperature), as an electrode for supercapacitors, exhibited a high specific capacitance of 225 F g^{-1} at a current density of 1 A g^{-1}. This specific capacitance may be maintained at 162 F g^{-1} and 10 A g^{-1}. The pair of oxidation and reduction peaks at approximately 0.4 V (quinone-type species (C = O)) was broad and extended to lower potentials (down to 0 V; N functionalities), indicating the excellent pseudocapacitive behavior of nitrogen-self-doped mesoporous carbons. The nitrogen-self-doped mesoporous carbons had good stability, with 93.92 % capacitance retention after 5000 cycles at a current density of 2 A g^{-1}.

✉ Bo Mu
mu-bo@163.com

1 College of Petrochemical Technology, Lanzhou University of Technology, Lanzhou 730050, China

Introduction

A capacitor is a small device that can provide quick bursts of energy. Capacitors are mostly known for powering laptops and hybrid cars, but these gadgets cannot store as much power as batteries [1, 2]. Meanwhile, supercapacitors are novel energy-storage components with huge potential storage capabilities. Supercapacitors can provide higher power density than chemical batteries and has many capacitor characteristics (e.g., quick charge/discharge and long cycle life) [3–5].

Electrode materials crucially affect supercapacitor performance. Porous carbons, the most widely used electrode materials for supercapacitors, have high specific surface area and excellent conductivity. Porous carbons are currently obtained by the carbonization of organic precursors (natural or synthetic), followed by physical or chemical activation. The precursors have wide-ranging sources, including biomaterials (cellulose, potato starch [6], as produced [7], and banana fiber [8, 9]), macromolecular compounds (phenolic resin [1], fragrant resin [10], ethylenediamine, and carbon tetrachloride [11]), and organic salts (e.g., potassium/sodium humate [12] and potassium/sodium citrate [13]). However, materials produced this way are made up almost exclusively of narrow pores. The mechanism of energy storage is based on the formation of an electrical double layer based on the electrode–electrolyte interface [14]. The electric-double-layer capacitance properties of carbon-based supercapacitors are often associated with the effects of specific surface area and porosity structure on the transmission of electrolyte ions, but sub-micropores (<1 nm) set a limit for the transmission for electrolyte ions [15–17]. Mesoporous-carbon materials prepared by the template

method avoid the disadvantages of sub-micropore materials because of the excellent porous structure. However, these procedures rely on the fabrication of sacrificial templates (mesoporous silica or surfactants), which are expensive, time consuming, and complicated to prepare and are thus unsuitable for large-scale production and industrial applications. Thus, the establishment of a simple, economic method of preparing mesoporous-carbon materials is the focus of the present study.

Traditional porous-carbon materials forming a double-layer structure for energy storage cannot meet the development needs of supercapacitors [18]. Thus, we should further enhance the capacitance properties of porous-carbon materials to promote supercapacitor development. Interestingly, doped porous-carbon materials as electrode materials can well improve the wetting of electrodes, conductive rate, and capacity through several techniques [19]. Some techniques include the incorporation of nitrogen groups into the carbon framework by the pyrolysis of biomass precursors containing a rich amount of these elements, thereby providing additional pseudocapacitance from the redox reaction of the heteroatom surface functionalities [20]. Given these unique properties, nitrogen-doped porous-carbon materials can satisfy the increasing demands for next-generation energy storage [21]. However, the synthesis of nitrogen-doped carbon materials involves the use of toxic and expensive synthetic precursors and/or requires post-treatment processing for the introduction of nitrogen or development of porosity [22]. The challenges encountered in the establishment of more environmentally friendly and cost-effective synthesis methods are increasingly being overcome through the use of naturally occurring renewable nitrogen-bearing biopolymers, including chitin [23], chitosan [24], and proteins [25]. Among these biomass proteins, keratin [26], silk fibroin [27], egg albumin [28], and gelatin [29] have been demonstrated to be nearly ideal precursors for the synthesis of N-doped carbon materials for electrochemical applications [29–31].

FAC is extensively used in the food industry as an additive and in medicine to treat iron-deficiency anemia in humans and animals. FAC is also used as a positive oral contrast agent in magnetic resonance imaging [32]. Two types of FAC exist and are known as FAC brown (Fig. 1) and FAC green. FAC-brown's contents of iron (16.5–18.5 %) and ammonia is 9 % more than that of FAC green (14.5–16 % iron; approximately 7.5 % ammonia). Thus, we select FAC brown as the carbon/nitrogen/oxygen precursor.

We researched nitrogen-self-doped mesoporous-carbon materials derived from FAC brown and used them as the carbon/nitrogen/oxygen precursor for supercapacitors. The effects of carbonization temperature on the nitrogen-doped mesoporous-carbon material microstructure, nitrogen content, and electrochemical properties were significant. The nitrogen-self-doped mesoporous carbons were then used as electrodes for high-performance supercapacitors, and their excellent
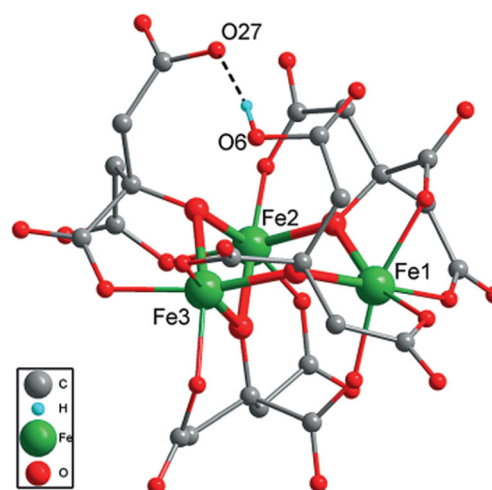

Fig. 1 Structure of $[Fe_3 (cit)_4H]^{6-}$

charge-storage properties were observed in 1 M H_2SO_4 aqueous solutions. We also showed a simple strategy for introducing nitrogen functional groups into the mesoporous carbons produced by this method.

Experimental

Synthesis of materials

The FAC brown used in the present work was purchased from Fuchen Industrial Corporation and used as received. Nitrogen-self-doped mesoporous carbons were prepared by the single-step carbonization of FAC brown. The prepared FAC-brown powder was ground, placed in a porcelain boat, and then heated in a horizontal tube furnace for up to 600, 700, 800, or 900 °C at a rate of 3 °C min^{-1}. The final temperature was maintained for a particular time (i.e., 2 h) under N_2 (99.999 %) flow. The resultant black substance was first washed with 1 M HCl solution to remove inorganic impurities and then with deionized water to reach neutral pH. After filtration, the product was dried at 80 °C, and the obtained porous-carbon materials were named FBNC-T. FB represents FAC brown (CAS Reg. No. 1332-98-5), N represents "nitrogen-self-doped," C represents mesoporous-carbon materials, and T represents carbonization temperature.

Structural characterization

The morphology of materials was investigated by field-emission scanning electron microscopy (FESEM; JSM-5600LV, JEOL) and high-resolution transmission electron microscopy (HRTEM; JEM-1200EX, JEOL). The crystalline structures of the materials were determined by powder X-ray diffraction (XRD; D/Max-2400, Rigaku). The nitrogen sorption isotherms of the porous-carbon materials were measured

using a Micromeritics ASAP 2020 sorptometer. The apparent surface area was calculated from the N_2 isotherms at relative pressures (P/P_o) from 0.06 to 0.20 by the Brunauer–Emmett–Teller (BET) method. Total pore volume (V_{total}) was determined from the amount of N_2 adsorbed at a relative pressure (P/P_o) of 0.97. Pore-size distribution was calculated using the slit/cylindrical nonlocal density functional theory model. Average pore size was calculated using the characteristic adsorption energy deduced by applying the Dubinin Radushkevich equation to the nitrogen-adsorption branch [33].

Electrochemical measurements

To prepare the working electrode, the nitrogen-self-doped mesoporous carbons were ground with polytetrafluoroethylene (5 wt.%) and then pressed onto steel mesh (1 cm × 1 cm) functioning as the current collector. The carbons were then dried in a vacuum at 80 °C for 12 h, and the working electrode was subsequently pressed at 15 MPa for 1–2 min. A conductive agent (such as acetylene black) was not required to prepare the working electrodes. Test samples were prepared in pellet form (diameter, 13 mm; thickness, 0.6 mm) at a pressure of 40 MPa.

Electrochemical measurements including CV, GCD, and EIS were performed under ambient conditions in 1 M H_2SO_4 aqueous solution by using a three-electrode system with nitrogen-self-doped mesoporous carbons as the working electrode, a platinum slice (1.5 cm^2) as the counter electrode, and a saturated calomel electrode as the reference electrode. GCD tests were performed at charge/discharge currents of 1–20 A g^{-1} over a potential window of 0 to 1 V. The specific capacitance C (F g^{-1}) of the samples was calculated as in Eq. (1):

$$C = \frac{I \times \Delta t}{m \times \Delta V} \quad (1)$$

where I is the constant discharging current (A), Δt is the discharge time (s) period for the potential change ΔV (V), and m (g) is the mass of nitrogen-self-doped mesoporous carbons in the electrode.

CV was performed at scan rates of 5–120 mV s^{-1} over the potential window of 0 to 1 V. The specific capacitance C (F g^{-1}) was also calculated from the CV curves according to Eq. (2):

$$C = \frac{\int I dV}{2 \times v \times m \times \Delta V} \quad (2)$$

where I is the current as a function of voltage, and v is the scan rate (V s^{-1}). EIS measurements were performed at the open-circuit potential with an AC amplitude of 5 mV within the frequency range of 10^{-2}–10^5 Hz.

Results and discussion

Figure 2 shows the XRD patterns of carbonization under different conditions. Nitrogen-self-doped mesoporous carbons under different carbonization temperatures had a similar structure. The diffraction peaks at $2\theta = 23.1°$ and $44.1°$ corresponded to the (002) and (101) planes of graphite diffraction crystal, respectively. No diffraction peaks of impurities could be detected. However, compared with the standard $2\theta = 26.6°$ of graphite, that of the sample obviously shifted to the left, which indicated that the interlamellar spacing between the (002) plane was extended according to Bragg's equation: $2d \cdot \sin\theta = \lambda$. Therefore, FBNC-700 exhibited an amorphous framework and low degree of graphitization. The low intensity (101) in the low-angle region was due to the fact that the nitrogen-self-doped mesoporous carbons had almost no carbon nanosheet structures. Similarly, FBNC-600/800/900 also presented amorphous structures. However, the peaks at $2\theta \approx 23.1°$ corresponded to the (002) planes of graphite diffraction crystal has obvious difference among FBNC-T. The XRD patterns also have been used to study the crystallinity of FBNC-T with different carbonization temperature. The strength of the peak could be closely intertwined with the crystallinity. The strength of the peak, the peaks at $2\theta \approx 23.1°$, of the XRD tested sample changes with of carbonization temperature increasing. Because the impurities have not full decompose at lower carbonization temperature, FBNC-600 has been in disorder and lower crystallinity. The FBNC-700 of decompose steadied with the carbonization temperature increasing. The strength of the peak, the peaks at $2\theta \approx 23.1°$, is stronger with the increase of the crystallinity. The development and growth of the structural properties of FBNC-T were affected seriously by the high temperature treatment. The crystal structure of FBNC-800 and FBNC-900 was destroyed, because mixed elements of functional groups react with the carbon and it tends to affect the structural properties.
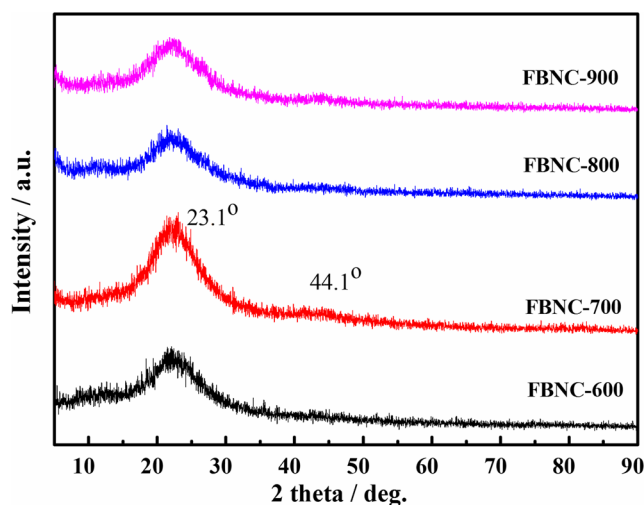
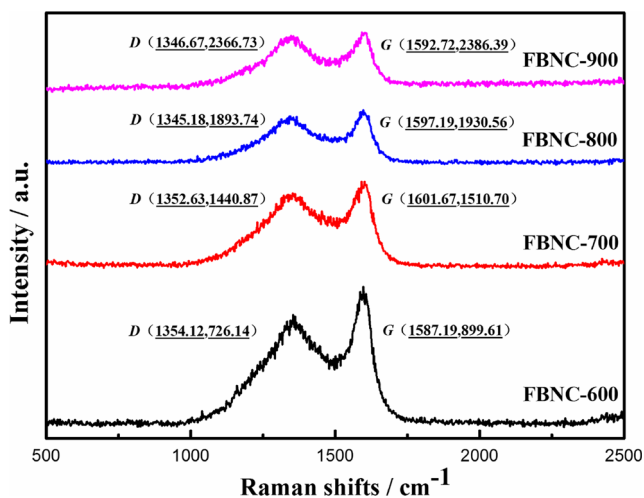

Fig. 2 Powder XRD pattern of FBNC-T

Fig. 3 Raman spectra of FBNC-T

was closely related to the degree of disorder of graphite structure and showed the graphitization degree of FBNC-T. With increased temperature, the D-band to G-band intensity ratio ($I_D/I_G < 1$) decreased. As received, the calculated I_D/I_G values of FBNC-900, FBNC-800, FBNC-700, and FBNC-600 were determined to be about 0.992, 0.981, 0.954, and 0.801, respectively. With increased temperature, the graphitizable extent of wood ceramics and ordering structure increased the I_D/I_G of FBNC-700 and made it higher than that of FBNC-600. Furthermore, the highly porous and disordered structure produced many defects in the nitrogen-self-doped mesoporous carbons, causing the I_D/I_G of FBNC-700 to be lower than those of FBNC-800 and FBNC-900. In addition, the size of graphitic carbon (La) was calculated according to the empirical equation La = $4I_G/I_D$. La of FBNC-600, FBNC-700, FBNC-800 and FBNC-900 are 4.032258, 4.07747197, 4.19287212, and 4.9937578 nm, respectively. These results illustrate that the FBNC-700 possess practically graphitized microstructure which is beneficial to fast electron transfer [31].

XPS analysis revealed that a significant fraction of the investigated carbons indicated the presence of three distinct peaks because of carbon, nitrogen, and oxygen in the

The Raman spectrum of FBNC-T (Fig. 3) showed characteristic D and G bands at about 1350 and 1590 cm^{-1}. The D band corresponded to an E$_{2g}$ mode of graphite and was related to the breathing mode of the ring, whereas the G band corresponded to the in-plane bond stretching motion of C sp2 atoms. The D-band to G-band intensity ratio ($I_D/I_G < 1$)
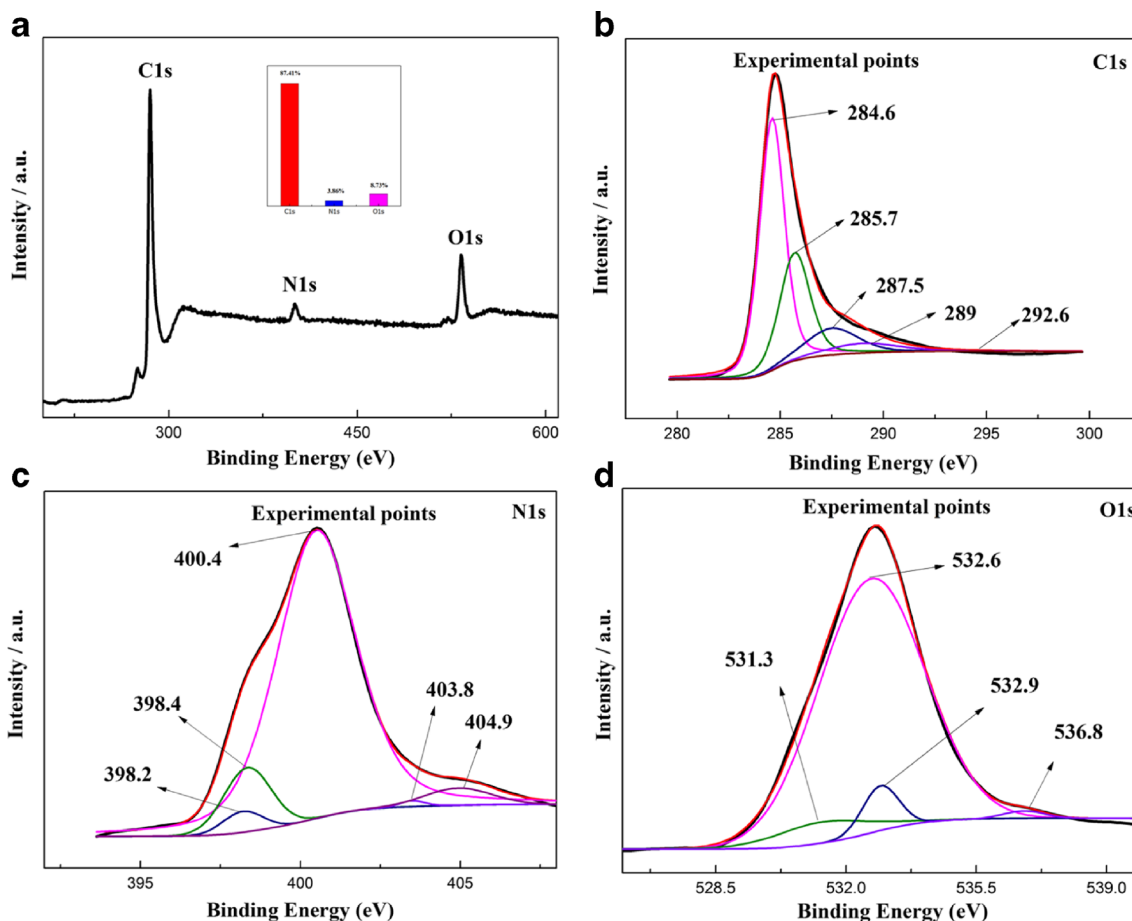
Fig. 4 **a** XPS survey, **b** C1s, **c** N1s, and **d** O1s XPS spectra of FBNC-700 after fitting

Table 1 XPS spectra of the FBNC-T

	XPS		
	C%	N%	O%
FBNC-600	88.91	4.42	6.67
FBNC-700	87.41	3.86	8.73
FBNC-800	92.91	1.97	5.12
FBNC-900	92.91	0.75	6.34

nitrogen-self-doped mesoporous carbon of FBNC-700. The carbon, nitrogen, and oxygen contents were calculated to be 87.41, 3.86, and 8.73 %, respectively. The nitrogen and oxygen groups can effectively improve the wettability of the carbon electrode material and increase the total capacity through the pseudocapacitance [34].

Analysis of Fig. 4c revealed that a significant fraction of N was surface accessible. To study in detail the contributions of particular nitrogen functionalities, we analyzed the XPS N1s core-level spectra. A standard deconvolution procedure using a Shirley background yielded five peaks centered at 398.2, 398.4, 400.4, 403.8, and 404.9 eV. These peaks were attributed to aromatic amides or imino compounds, pyridinic nitrogen (N-6), pyrrolic nitrogen (N-5), oxidized nitrogen (N-X), and the chemisorption of nitrogen oxides [34–36].

The core-level O1s spectra of the obtained carbons are presented in Fig. 4d. The interpretation of the O1s spectra was not straightforward because of the very narrow range of binding energies and the possible overlapping of different components. In this study, we deconvoluted the O1s spectra into four components. The three major peaks were assigned to isolated carbonyl groups (531.3 eV), carbonyl groups in anhydrides or carboxyls (532.6 eV), and ether or hydroxyl (532.9 eV). The outermost components (536.7 eV) were used to improve the fit. The component, centered at 536.7 eV, was typically attributed to chemisorbed oxygen or water [34, 37]. The presence of O- and N-containing groups on the carbon surface was confirmed by the core-level C1s spectra (Fig. 4b). In addition to the primary signal of graphitic $sp2$-bonded carbon (at 284.6 eV), the spectra contained asymmetric tails that could be fitted with several peaks attributed to C–O and C–N functionalities (285.7 eV), carbonyl groups (287.5 eV), carboxyl groups (289 eV), carbonates or a satellite line of the C = O component (296.0 eV), and shake-up satellites related to the π–π* transition (292.6 eV) [38, 39].

The nitrogen content was strongly dependent on the carbonization temperature, i.e., the samples carbonized at the higher temperature contained less nitrogen. It was obvious that the N% had been paid attention to decrease (Tables 1 and 2). Furthermore, FBNC-700 has more content of nitrogen and oxygen. It is good for improving electron transfer and resulting in a corresponding increase in specific capacitance.

The FESEM images of FBNC-700 (Fig. 5a) displayed nitrogen-self-doped mesoporous-carbon materials stacked by nanospherical particles (Fig. 5b). Obviously, nanospherical particles piled up and produced many pores through the defect. To further access the internal structure of the nitrogen-self-doped mesoporous-carbon materials, HRTEM was used. The HRTEM image in Fig. 5c confirmed that the accumulation of nanospherical particles included micropores and mesopores. The magnified HRTEM images in Fig. 5d showed that the structure of the nitrogen-self-doped mesoporous-carbon materials was amorphous.

The porous structure of the nitrogen-self-doped mesoporous-carbon materials obtained from the nitrogen sorption isotherms is shown in Fig. 6. The isotherm profiles exhibited well-defined capillary condensation steps typical of mesoporous materials (type-*IV* (a) isotherm), indicating that the porosity was mainly made up of mesopores [40]. The well-developed mesoporosity helped electrolytes to be quickly stored in the charge/discharge process. At a low pressure (close to 0), the adsorbed N_2 volume did not significantly increase. In this case, the initial monolayer–multilayer adsorption on the mesopores walls, which took the same path as the corresponding part of a type-II isotherm, was followed by pore condensation. The amount of micropores in the nitrogen-self-doped mesoporous-carbon materials was not negligible. Test by Raman, carbonization temperature is closely correlated with the graphitization of carbon materials, and thereby affecting the carbon materials ordered, such as pore structure. At a low carbonization temperature, the hysteresis loop (H2(b)) concentration appeared in high pressure (0.45–0.9) show that FBNC-600 has mesoporous with larger diameter (Fig. 6). At a low pressure (close to 0), the adsorbed N_2 volume did not significantly increase show that FBNC-600 lack of micropore structure. The phenomenon can be observed

Table 2 BET surface area and porosity characteristics of the FBNC-T

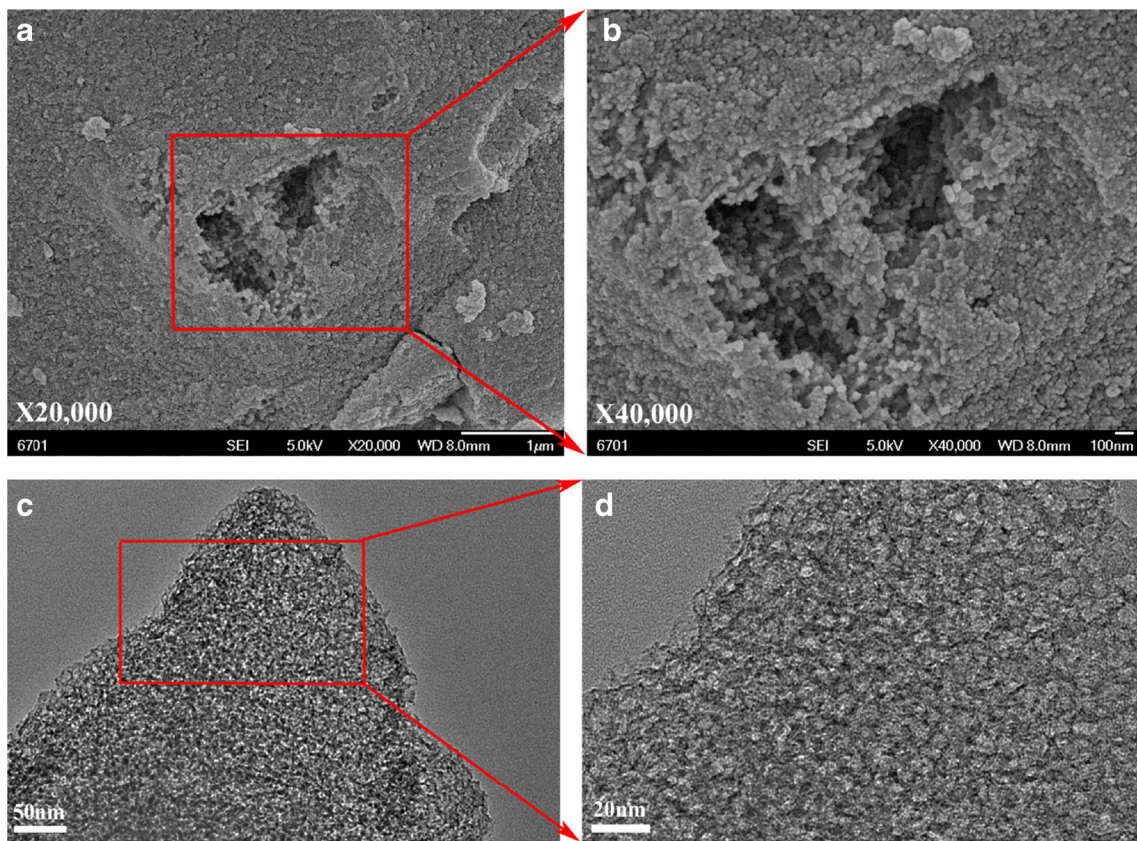| Active materials	S_{BET} ($m^2\,g^{-1}$)	$S_{micropore}$ ($m^2\,g^{-1}$)	$V_{total\ pore}$ ($cm^3\,g^{-1}$)	$V_{micropore}$ ($cm^3\,g^{-1}$)	$D_{average}$ (nm)
FBNC-600	524	201	1.0901	0.0911	8.33
FBNC-700	1021	153	1.3770	0.0651	5.39
FBNC-800	1131	106	2.0552	0.0392	7.27
FBNC-900	912	88	1.8495	0.0329	8.12

Fig. 5 a, b FESEM images, c, d HRTEM images of FBNC-700 at different magnifications

clearly in the Fig. 7. As the temperature rises, the adsorption increased at low pressure show that increased number of micropores. Because of the number of micro-porous directly affect the surface area of materials, FBNC-700 and FBNC-800 has a larger surface area. The hysteresis loop (H2(a)) concentration appeared in a narrow range of pressure (0.4–0.85) show that FBNC-700 has mesoporous with a narrow range of diameter (Fig. 6). At high pressure (close to 1.0), the adsorbed N_2 volume did not significantly increase show that FBNC-700 had almost no macropores. The hysteresis

loop observed at moderate pressure (0.45–0.95) revealed the presence of slit-shaped mesopores in FBNC-800 and FBNC-900. As the temperature further rises, the hysteresis loop (H3) be arising in the pressure of ~0.5. Because of the physical process of the pore enlargement, the mesoporous appeared in a wide range of diameter (Fig. 6) and the hysteresis loop persisted in a wide range of pressure. Because of temperature further rises, the diameter of pore is made increase. The adsorbed N_2 volume of FBNC-900 is lower than FBNC-700 or FBNC-800 because the number of micropores decreased.
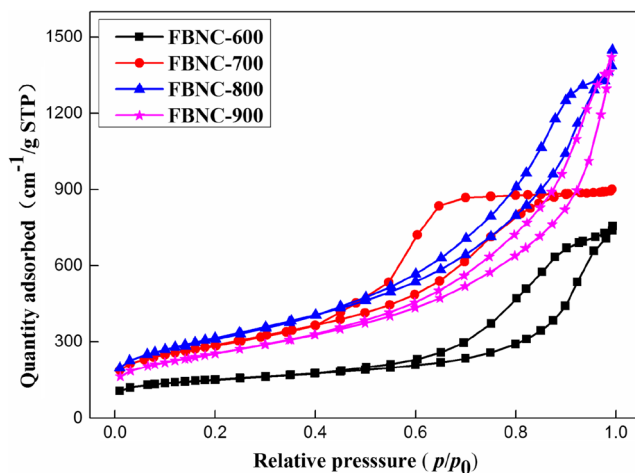
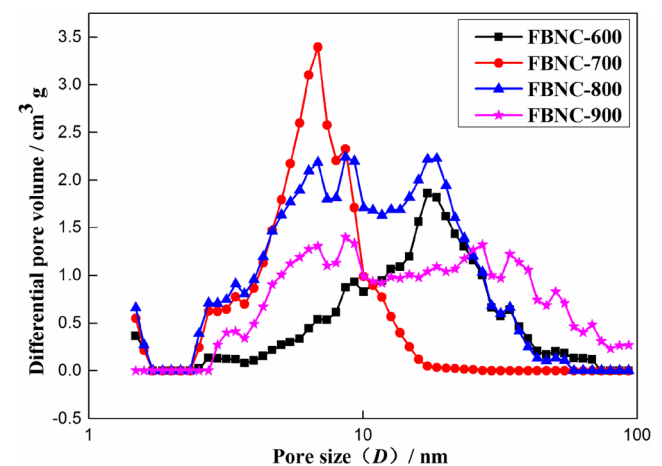

Fig. 6 Nitrogen-adsorption isotherms of FBNC-T

Fig. 7 The pore size distribution of FBNC-T

The diameter of micropores is made increase lead to the hysteresis loop (H3) be arising in the pressure of ~0.4. At high pressure (close to 1.0), the adsorbed N_2 volume did significantly increase show that FBNC-900 had more macropores because mesoporous transformed into macropores. And the surface area of FBNC-900 is reduced significantly. This finding was confirmed by the PSDs in Fig. 7, which clearly revealed that the porosity of the nitrogen-self-doped mesoporous-carbon materials was mainly made up of large mesopores. The broad hump-like feature corresponding to

the mesopores of FBNC-700 was found to be accompanied by two well-separated peaks: a sharp one located at approximately 2 nm and a broader one located at approximately 9 nm. Notably, similar bimodal distributions of micropores have been reported for the majority of activated carbons. The micropores formed in the carbon walls of mesopores as a result of shrinkage hindering or chemical activation in a thin film present on the surface of the silica particles. The mesoporosity of the nitrogen-self-doped mesoporous-carbon materials was generated almost exclusively by the selective removal of the
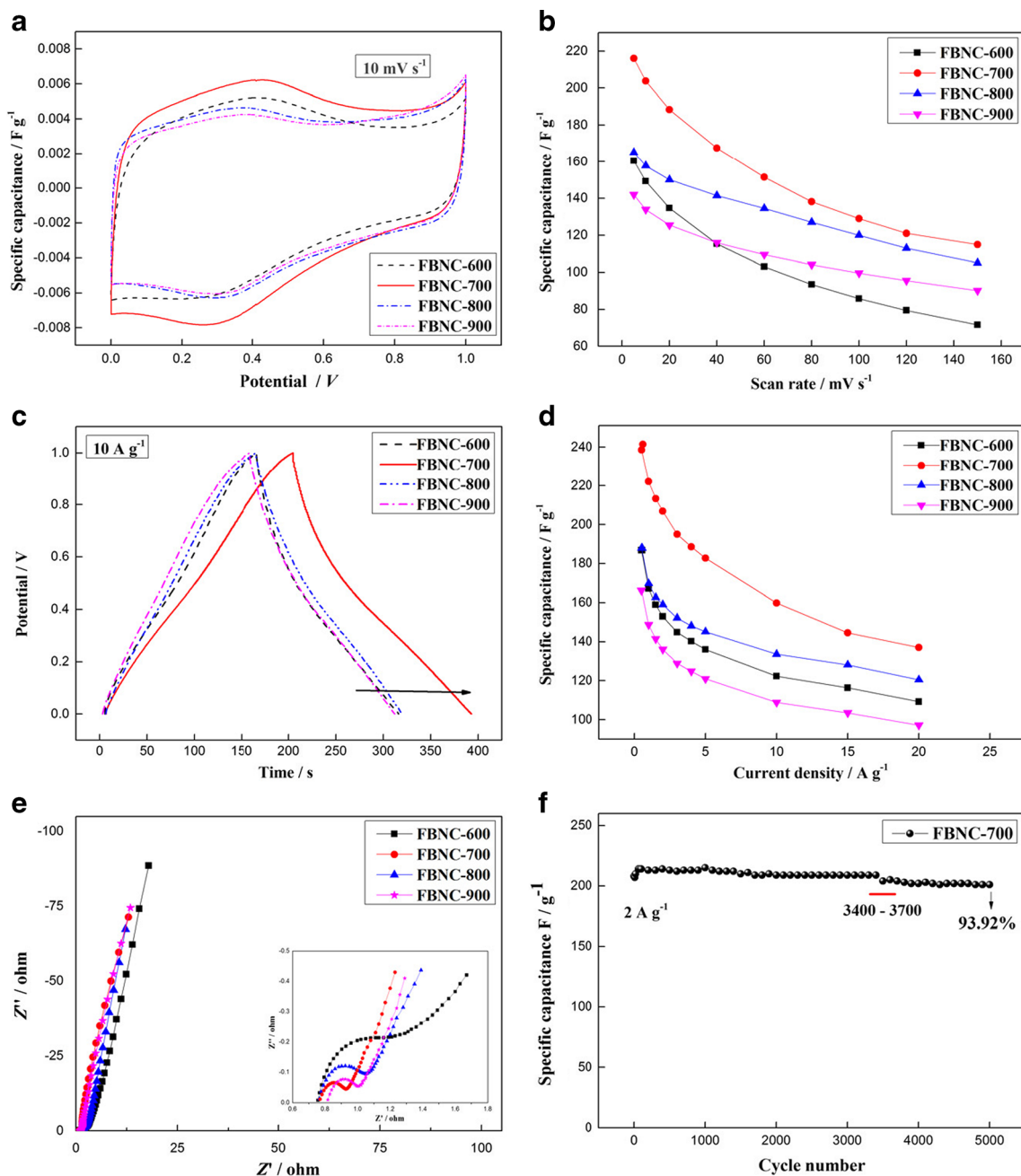

Fig. 8 **a** Comparison of cyclic voltammograms results between the electrolyte of pure H_2SO_4 (1 M). CV curves at 10 mV s^{-1}. **b** Specific capacitance vs. scan rates. **c** FBNC-T curves at 10 A g^{-1}. **d** Specific capacitances calculated from FBNC-T curves. **e** Nyquist plot. **f** Cyclic stability

Table 3 The CV profiles of FBNC-T at different scan rate

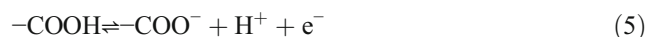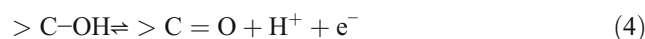| Current density/A g^{-1}	5	10	20	40	60	80	100	120	150
FBNC-600	160	149	135	115	103	93	86	79	72
FBNC-700	216	204	188	167	152	138	127	117	105
FBNC-800	165	158	150	141	135	130	125	121	115
FBNC-900	142	134	126	115	109	104	100	95	90

iron-oxide nanoparticles present in the carbon/inorganic composites. Thus, the iron-oxide nanoparticles embedded within the carbon matrix can be considered as an endotemplate material, and the nanovoids remaining after their dissolution can be considered as the mesopores.

FBNC-600, FBNC-700, FBNC-800, and FBNC-900 displayed total BET surface areas of 524, 1021, 1131, and 912 m^2 g^{-1}, as well as total pore volumes of 1.09, 1.38, 2.06, and 1.85 cm^3 g^{-1}, respectively. T-plot results showed that the micropore volumes of FBNC-600, FBNC-700, FBNC-800, and FBNC-900 may be estimated to be 0.09, 0.65, 0.39, and 0.33 cm^3 g^{-1}, respectively. However, the contributions of micropores and small mesopores were higher, and pores representing unfilled interparticle cavities (4–10 nm) were present. The total BET surface areas of FBNC-700 were less than FBNC-800. Interestingly, the electrochemical properties of FBNC-700 were better than those of FBNC-800 because more micopores existed in FBNC-700 and the pores were bimodally distributed.

N doping is known to contribute to capacitance through a pseudocapacitive effect originating from fast Faradaic redox reactions and through a non-Faradaic effect resulting from the increased electron density, which increases the space-charge capacitance. Graphitic nitrogen effectively enhances the space-charge capacitance, whereas "edge" nitrogen (i.e., N-6 and N-5) contributes most markedly to pseudocapacitance. Among the oxygen functionalities, only quinone groups have been confirmed to significantly contribute to pseudocapacitance. The pseudocapacitive response due to N and O functionalities may be strongly suppressed in alkaline media [41].

The electrochemical properties of FBNC-T were evaluated in 1 M H$_2$SO$_4$ aqueous solutions by using a trielectrode system through CV, GCD, and EIS. Figure 8a shows the CV

profiles of FBNC-T at a scan rate of 10 mV s^{-1}. The CVs recorded in the H$_2$SO$_4$ electrolyte (Fig. 8a) exhibited a pair of oxidation and reduction peaks at approximately 0.4 V, which could be assigned to quinone-type species, thereby confirming the presence of C = O. And other oxygen-containing functional groups could take place to generate the pseudo capacitance by the following redox reactions. In addition, oxygen groups may improve carbon wettability of the internal structure of micropores in the carbon electrodes, thus resulting in a corresponding increase in specific capacitance [42, 43].

$$> C = O + e^+ \rightleftharpoons \; > C-O^- \qquad (3)$$

$$> C-OH \rightleftharpoons \; > C = O + H^+ + e^- \qquad (4)$$

$$-COOH \rightleftharpoons -COO^- + H^+ + e^- \qquad (5)$$

where > C stands for the carbon network [44].

These peaks were very broad and extended to lower potentials (down to 0 V), which can be attributed to Faradaic redox reactions involving N functionalities by the following redox reactions. The Faraday reactions take place at the edges of graphene sheets on N groups have no faradaic activity; however, they show enhancing effects on the capacitance due to their positive charge and thus an improved electron transfer.

$$> C = NH + 2e^- + 2H \rightleftharpoons \; > CH-NH_2 \qquad (6)$$

$$> C-NHOH + 2e^- + 2H^+ \rightleftharpoons \; > C-NH_2 + H_2O \qquad (7)$$
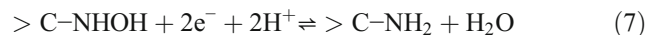
where > C stands for the carbon network [45].

Comparatively, FBNC-700 displayed the largest integrated area surrounded by CV curves, indicating that this material had the largest specific capacitance (Tables 3 and 4). The specific capacitances of FBNC-600, FBNC-700, FBNC-800, and FBNC-900 calculated from the CV curves at various scan rates are shown in Fig. 8b. Given their different BET surface areas, porous structures, and transmission of electrolytic ions between the surface of the electrode material and electrolyte, FBNC-700 exhibited the best electrochemical performance among the materials tested. The specific capacitance of FBNC-700 decayed by 45 % with increased sweep rate from 5 to 160 mV s^{-1}. In H$_2$SO$_4$ electrolyte, the specific capacitance retention ratio was lower. This finding was consistent with previous ones and suggested that the Faradaic redox

Table 4 The GCD curves of FBNC-T measured at different current density

Current density/A g^{-1}	0.5	1	1.5	2	3	4	5	10	15	20
FBNC-600	182	164	156	150	139	131	124	100	85	72
FBNC-700	242	225	216	209	197	191	185	162	146	138
FBNC-800	188	170	162	159	152	148	145	134	128	120
FBNC-900	166	149	141	136	129	125	121	109	103	97

reactions responsible for the pseudocapacitive effect in an H_2SO_4 electrolyte were insufficiently fast to effectively contribute to quick charge/discharge operations [46, 47].

Figure 8c demonstrates the GCD curves of FBNC-600, FBNC-700, FBNC-800, and FBNC-900 measured at a current density of 10 A g^{-1}. The profiles of these curves showed that slight deviation from a linear shape observed from charge/discharge branches further confirmed the existence of substantial faradaic capacitance for the samples. Meanwhile, a series of specific capacitances calculated from the GCD curves is indicated in Fig. 8d. FBNC-700 clearly had good electrochemical performance and can retain 64.66 % of its capacitance with increased current density from 1 A g^{-1} (225 F g^{-1}) to 10 A g^{-1} (162 F g^{-1}). The decrease in capacitance registered from low to high discharge current due to the increase in ohmic resistance was caused by an ion "traffic jam." In addition, considering diffusion kinetics, narrower pores made the ions more slowly diffuse. A high capacitance retention of 93.92 % was obtained even after charging/discharging for 5000 times, as shown in Fig. 8e. Obviously, a rapid decay process occurred between 3400 and 3500 from the discharge cycle because of oxygen/nitrogen functional decomposition caused by the reduced pseudocapacitance.

Figure 8f shows the Nyquist plots of FBNC-600, FBNC-700, FBNC-800, and FBNC-900. Obviously, the Nyquist plots were nearly vertical in the low-frequency region, indicating a relatively ideal capacitive performance of the materials. The high-frequency intersection of the plot with the X-axis represented the alternating current equivalent series resistance (AC-ESR), which was associated with the resistance of the material, the separator, and the contact between materials and current collector. The AC-ESR of FBNC-700 was 0.756, which was lower than that of others samples (the AC-ESR of FBNC-600, FBNC-800, and FBNC-900 were 0.764, 0.769, and 0.817 Ω, respectively.). The low AC-ESR was mainly due to the good electrical conductivity. The radius of the semicircle represented the pseudocharge-transfer resistance. Obviously, FBNC-700 had a smaller radius of semicircle than FBNC-600, FBNC-800, and FBNC-900's because of the hierarchical mesoporous network (bimodal pore structure). Based on the results presented, FBNC-700 had the behavior of supercapacitors close to that of an ideal capacitor.

Conclusion

We demonstrated the synthesis of nitrogen-self-doped mesoporous carbons with a large BET surface area of up to 1021 m^2 g^{-1}, bimodal porosity (pores centered at approximately 2 and 9 nm), and nitrogen-self-doped (3.86 %) using FAC as the carbon/nitrogen/oxygen precursor. The prepared nitrogen-self-doped mesoporous carbons exhibited a strong ability to accumulate charge (up to 225 F g^{-1} at 1 A g^{-1}) and excellent pseudocapacitance (the shape of the CVs recorded showed that pseudocapacitance was generated through faradaic redox reactions involving both N and O functionalities) in 1 M H_2SO_4 electrolytes. Moreover, this work about fabricating nitrogen-self-doped mesoporous carbons through this method can serve as a foundation for further research on the direct carbonization of organic salts as supercapacitor electrode materials.

References

1. Gu W, Yushin G (2013) Review of nanostructured carbon materials for electrochemical capacitor applications: advantages and limitations of activated carbon, carbide-derived carbon, zeolite-templated carbon, carbon aerogels, carbon nanotubes, onion-like carbon, and graphene. Wiley Interdisciplinary Reviews Energy & Environment 3(5):424–473
2. Service RF (2006) Materials science. New 'supercapacitor' promises to pack more electrical punch. Science 313(5789):902–902
3. Mahon PJ, Paul GL, Keshishian SM, Vassallo AM (2000) Measurement and modelling of the high-power performance of carbon-based supercapacitors. J Power Sources 91(1):68–76
4. Qu D (2002) Studies of the activated carbons used in double-layer supercapacitors. J Power Sources 109(2):403–411
5. Arbizzani C, Mastragostino M, Soavi F (2001) New trends in electrochemical supercapacitors. J Power Sources 100(1–2):164–170
6. SH D, Wang LQ, XT F, Chen MM, Wang CY (2013) Hierarchical porous carbon microspheres derived from porous starch for use in high-rate electrochemical double-layer capacitors. Bioresour Technol 139(13):406–409
7. Chen W, Zhang H, Huang Y, Wang W (2010) A fish scale based hierarchical lamellar porous carbon material obtained using a natural template for high performance electrochemical capacitors. J Mater Chem 20(23):4773–4775
8. Liu B, Zhang L, Qi P, Zhu M, Wang G, Ma Y, Guo X, Chen H, Zhang B, Zhao Z (2016) Nitrogen-doped banana peel–derived porous carbon foam as binder-free electrode for supercapacitors. Nanomaterials 6(1)
9. Lotfabad EM, Ding J, Cui K, Kohandehghan A, Kalisvaart WP, Hazelton M, Mitlin D (2014) High-density sodium and lithium ion battery anodes from banana peels. ACS Nano 8(7):7115–7129
10. Jurewicz K, Frackowiak E, Béguin F (2004) Towards the mechanism of electrochemical hydrogen storage in nanostructured carbon materials. Applied Physics A 78(7):981–987
11. Yunpu Z, Yuqian D, Dongyuan Z, Fulvio PF, Mayes RT, Sheng D (2011) Carbon materials for chemical capacitive energy storage. Adv Mater 23(42):4828–4850
12. Luo HM, Yang YF, Chen YZ, Zhang JQ, Zhao X (2015) Structure and electrochemical performance of highly porous carbons by single-step potassium humate carbonization for application in supercapacitors. J Appl Electrochem 46(1):113–121
13. Sevilla M, Fuertes AB (2013) A general and facile synthesis strategy towards highly porous carbons: carbonization of organic salts. J Mater Chem A 1(44):13738–13741
14. Liu X, Chang F, Xu L, Yang Y, He Y, Liu Z (2006) Synthesis and characterization of a new nanoporous carbon material with a bimodal pore system. Carbon 44(1):184–187

15. Salitra G, Soffer A, Eliad L, Cohen Y, Aurbach D (2000) Carbon electrodes for double-layer capacitors I. Relations between ion and pore dimensions. J Electrochem Soc 147(7):2486–2493

16. Eliad L, Pollak E, Levy N, Salitra G, Soffer A, Aurbach D (2006) Assessing optimal pore-to-ion size relations in the design of porous poly(vinylidene chloride) carbons for EDL capacitors. Appl Phys A Mater Sci Process 82(82):607–613

17. Lozano-Castello D, Cazorla-Amoros D, Linares-Solano A (2003) Influence of pore structure and surface chemistry on electric double layer capacitance in non-aqueous electrolyte. Carbon 9(9):1765–1775

18. Hang S (1996) Activated carbons and double layer capacitance. Electrochim Acta 41(10):1633–1639

19. Jurewicz K, Pietrzak R, Nowicki P, Wachowska H (2008) Capacitance behaviour of brown coal based active carbon modified through chemical reaction with urea. Electrochim Acta 53(16):5469–5475

20. Wang RT, Lang JW, Yan XB (2014) Effect of surface area and heteroatom of porous carbon materials on electrochemical capacitance in aqueous and organic electrolytes. Science China. Chemistry 57(11):1–9

21. Frackowiak E, Lota G, Machnikowski J, Vix-Guterl C, Béguin F (2006) Optimisation of supercapacitors using carbons with controlled nanotexture and nitrogen content. Electrochim Acta 51(11):2209–2214

22. Wood KN (2014) Recent progress on nitrogen/carbon structures designed for use in energy and sustainability applications. Energy & Environmental Science 7(4):1212–1249

23. White RJ, Antonietti M, Titirici MM (2009) Naturally inspired nitrogen doped porous carbon. J Mater Chem 19(45):8645–8650

24. Wang B, Tian C, Wang L, Wang R, Fu H (2010) Chitosan: a green carbon source for the synthesis of graphitic nanocarbon, tungsten carbide and graphitic nanocarbon/tungsten carbide composites. Nanotechnology 21(2):025606–025606

25. Olejniczak A, Lezanska M, Wloch J, Kucinska A, Lukaszewicz JP (2013) Novel nitrogen-containing mesoporous carbons prepared from chitosan. J Mater Chem 1(31):8961–8967

26. Si W, Zhou J, Zhang S, Li S, Xing W, Zhuo S (2013) Tunable N-doped or dual N, S-doped activated hydrothermal carbons derived from human hair and glucose for supercapacitor applications. Electrochim Acta 107(3):397–405

27. Kim YJ, Abe Y, Yanagiura T, Park KC, Shimizu M, Iwazaki T, Nakagawa S, Endo M, Dresselhaus MS (2007) Easy preparation of nitrogen-enriched carbon materials from peptides of silk fibroins and their use to produce a high volumetric energy density in supercapacitors. Carbon 45(10):2116–2125

28. Young Soo Y, Se Youn C, Jinyong S, Byung Hoon K, Sung-Jin C, Seung Jae B, Suk HY, Yongsug T, Yung Woo P, Sungjin P (2013) Microporous carbon nanoplates from regenerated silk proteins for supercapacitors. Adv Mater 25(14):1993–1998

29. Li Z, Xu Z, Tan X, Wang H, Holt CMB, Stephenson T, Olsen BC, Mitlin D (2013) Mesoporous nitrogen-rich carbons derived from protein for ultra-high capacity battery anodes and supercapacitors. Energy Environ Sci 6(3):871–878

30. Dutta S, Bhaumik A, Wu KC-W (2014) Hierarchically porous carbon derived from polymers and biomass: effect of interconnected pores on energy applications. Energy & Environmental Science 7(11):3574–3592

31. An H, Li Y, Long P, Gao Y, Qin C, Cao C, Feng Y, Feng W (2016) Hydrothermal preparation of fluorinated graphene hydrogel for high-performance supercapacitors. J Power Sources 312(30):146–155

32. Tenne D, Bogoslavsky B, Bino A (2015) Ferric ammonium citrate—What's in it? Ber Dtsch Chem Ges 2015(25):4159–4161

33. Stoeckli HF, Rebstein P, Ballerini L (1990) On the assessment of microporosity in active carbons, a comparison of theoretical and experimental data. Carbon 28(6):907–909

34. Pels J, Kapteijn F, Moulijn J, Zhu Q, Thomas K (1995) Evolution of nitrogen functionalities in carbonaceous materials during pyrolysis. Carbon 33(11):1641–1653

35. Raymundo-Piñero E, Cazorla-Amorós D, Linares-Solano A, Find J, Wild U, Schlögl R (2002) Structural characterization of N-containing activated carbon fibers prepared from a low softening point petroleum pitch and a melamine resin. Carbon 40(4):597–608

36. Huang X, Wang Q, Chen XY, Zhang ZJ (2015) N-doped nanoporous carbons for the supercapacitor application by the template carbonization of glucose: the systematic comparison of different nitridation agents. J Electroanal Chem 748:23–33

37. Schmiers H, Friebel J, Streubel P, Hesse R, Köpsel R (1999) Change of chemical bonding of nitrogen of polymeric N-heterocyclic compounds during pyrolysis. Carbon 37(12):1965–1978

38. Desimoni E, Casella GI, Morone A, Salvi AM (1990) XPS determination of oxygen-containing functional groups on carbon-fibre surfaces and the cleaning of these surfaces. Surface & Interface Analysis 15(10):627–634

39. Kozlowski C, Sherwood PMA (1986) X-ray photoelectron spectroscopic studies of carbon fibre surfaces vii-electrochemical treatment in ammonium salt electrolytes. Carbon 24(3):357–363

40. Thommes M, Kaneko K, Neimark AV, Olivier JP, Rodriguez-Reinoso F, Rouquerol J, Sing KS (2015) Physisorption of gases, with special reference to the evaluation of surface area and pore size distribution (IUPAC Technical Report. Pure Appl Chem 87(9–10):1051–1069

41. Lee YH, Chang KH, CC H (2013) Differentiate the pseudocapacitance and double-layer capacitance contributions for nitrogen-doped reduced graphene oxide in acidic and alkaline electrolytes. J Power Sources 227(4):300–308

42. Li N, Ma X, Zha Q, Kim K, Chen Y, Song C (2011) Maximizing the number of oxygen-containing functional groups on activated carbon by using ammonium persulfate and improving the temperature-programmed desorption characterization of carbon surface chemistry. Carbon 49(15):5002–5013

43. Li H, Ha X, Zhu S, Wen Z, Wang R (2006) Preparation, structural characterization, and electrochemical properties of chemically modified mesoporous carbon. Microporous Mesoporous Mater 96(1):357–362

44. Hsieh C-T, Teng H (2002) Influence of oxygen treatment on electric double-layer capacitance of activated carbon fabrics. Carbon 40(5):667–674

45. Hulicova-Jurcakova D, Seredych M, Lu GQ, Bandosz TJ (2009) Combined effect of nitrogen-and oxygen-containing functional groups of microporous activated carbon on its electrochemical performance in supercapacitors. Adv Funct Mater 19(3):438–447

46. Lu H, Dai W, Zheng M, Li N, Ji G, Cao J (2012) Electrochemical capacitive behaviors of ordered mesoporous carbons with controllable pore sizes. J Power Sources 209(7):243–250

47. Yamada H, Nakamura H, Nakahara F, Moriguchi I, Kudo T (2006) Electrochemical study of high electrochemical double layer capacitance of ordered porous carbons with both meso/macropores and micropores. Jphyschemc 111:227–233